

**OPEN ACCESS**

## Editors' Choice—State of Charge Dependent Resistance Build-Up in Li- and Mn-Rich Layered Oxides during Lithium Extraction and Insertion

To cite this article: Tobias Teufl *et al* 2019 *J. Electrochem. Soc.* **166** A1275

View the [article online](#) for updates and enhancements.



# State of Charge Dependent Resistance Build-Up in Li- and Mn-Rich Layered Oxides during Lithium Extraction and Insertion

Tobias Teuffl,<sup>1,2,z</sup> Daniel Pritzl,<sup>1,2,\*</sup> Sophie Solchenbach,<sup>1,2,\*</sup> Hubert A. Gasteiger,<sup>2,\*\*</sup> and Manuel A. Mendez<sup>1</sup>

<sup>1</sup>BASF SE Ludwigshafen, New Battery Materials and Systems, D-67056 Ludwigshafen, Germany

<sup>2</sup>Chair of Technical Electrochemistry, Department of Chemistry and Catalysis Research Center, Technical University of Munich, D-85748 Garching, Germany

Lithium- and manganese-rich layered oxide-based cathode active materials (often referred to as HE-NCM) exhibit high reversible specific capacity ( $\approx 250$  mAh/g) and could improve future lithium-ion batteries in terms of energy density and safety, while offering lower cost. Unfortunately, drawbacks such as voltage-fading, hysteresis, and increasing cathode impedance over charge/discharge cycling have so far hindered its commercialization. In this study, we examine the reasons and the implications of the high resistance build-up of this material in graphite//HE-NCM full-cells. Impedances/resistance were obtained either by electrochemical impedance spectroscopy (EIS) with a micro-reference electrode or by current pulse measurements (so-called direct-current internal-resistance (DCIR) measurements). These data show that the so-called activation of the material above 4.5 V vs.  $\text{Li}^+/\text{Li}$  leads to an asymmetric high charge-transfer impedance at low state-of-charge (SOC) between charge and discharge, manifested as an anomalous cell resistance hysteresis which increases over cycling and with increasing upper cutoff potentials. These findings are rationalized by reversible transition-metal migration phenomena.

© The Author(s) 2019. Published by ECS. This is an open access article distributed under the terms of the Creative Commons Attribution Non-Commercial No Derivatives 4.0 License (CC BY-NC-ND, <http://creativecommons.org/licenses/by-nc-nd/4.0/>), which permits non-commercial reuse, distribution, and reproduction in any medium, provided the original work is not changed in any way and is properly cited. For permission for commercial reuse, please email: [oa@electrochem.org](mailto:oa@electrochem.org). [DOI: 10.1149/2.1131906jes]



Manuscript submitted February 15, 2019; revised manuscript received March 29, 2019. Published April 16, 2019.

To address the future demand for sustainable and environmental friendly transportation, alternatives to classical combustion engines are required and lithium ion batteries have become an attractive option, as they offer high energy densities and as they have already been proven in consumer electronics for many years.<sup>1-3</sup> When Sony commercialized the first lithium-ion battery in the early 1990's, it was based on the use of a graphite anode and a  $\text{LiCoO}_2$  (LCO) cathode.<sup>3,4</sup> Since then, much effort has been expended in developing and implementing new cathode active materials (CAMs) which would offer higher capacities, and promising performance has been shown by stoichiometric layered lithium-nickel-cobalt-manganese-oxides ( $\text{LiNi}_x\text{Co}_y\text{Mn}_z\text{O}_2$ , with  $x+y+z=1$ ), commonly referred to as NCMs, which also offer the possibility to finetune their properties by changing the ratios between the transition metals.<sup>5-7</sup> Initially, NCM materials with a Ni:Co:Mn ratio of 1:1:1 were investigated (referred to as NCM-111), while more recently nickel-rich materials (e.g., Ni:Co:Mn = 8:1:1, referred to as NCM-811) have been favored, as they offer high capacities at more moderate upper cutoff voltages.<sup>8</sup> However, even with nickel-rich materials, a reversible capacity of 200 mAh/g cannot be exceeded due to structural instabilities at high degrees of delithiation, leading to oxygen release from the surface<sup>9</sup> and, ultimately, to a collapse of the bulk structure.<sup>10</sup>

A promising attempt to further increase the energy density of layered oxide based CAMs are composite materials consisting of  $x \text{Li}_2\text{MnO}_3 \cdot 1-x \text{LiMO}_2$  ( $M = \text{Ni}, \text{Co}, \text{Mn}$ ), so-called overlithiated NCM materials, also referred to as high-energy NCM (HE-NCM).<sup>11-13</sup> A special feature of these materials is the long activation plateau occurring at 4.5 V vs.  $\text{Li}^+/\text{Li}$  during the first charge cycle, whereby charging beyond this plateau leads to high reversible capacities of around 250 mAh/g.<sup>11,14</sup> As the high capacities after activation cannot be explained by classical cationic redox, the material has been extensively studied, seeking to find an explanation for the high reversible capacities. Initially, the activation plateau was associated with a bulk oxygen release from the  $\text{Li}_2\text{MnO}_3$  domain, leading to electrochemically active  $\text{LiMnO}_2$ ,<sup>11-17</sup> and it was suggested that the oxygen release also would initiate phenomena like the 1 V hysteresis of the material<sup>18</sup> as well

as the observed voltage-fading over the course of charge/discharge cycling, ultimately leading to a spinel structure in the bulk of the material.<sup>12,13,18-20</sup> Even though it is still subject of ongoing discussions, more recent studies suggest that the bulk and the surface of HE-NCM show distinctly different behaviors: while oxygen release and spinel formation was shown to occur only in surface-near regions,<sup>21-24</sup> there is strong evidence that anionic oxygen redox in the bulk of HE-NCM materials is the cause for the high reversible capacities.<sup>21,22,25-28</sup> Furthermore, it is suggested that irreversible delithiation of the transition-metal layer occurs during the activation plateau<sup>29,30</sup> and triggers disorder and transition-metal migration within the bulk material, which might be the explanation for the charge/discharge hysteresis and for the voltage fading of activated HE-NCM.<sup>31-35</sup>

Besides voltage-fading and charge/discharge hysteresis, another major drawback of HE-NCM that has hindered its commercialization so far is the high impedance of the material,<sup>36-40</sup> particularly at low state-of-charge (SOC).<sup>37,38,41</sup> On the one hand, it has been shown in the literature that sluggish bulk diffusion leads to poor rate capabilities and high resistances,<sup>40,42</sup> on the other hand, there is also clear evidence that restructuring in surface-near regions contributes to a resistive surface layer which slows down lithium diffusion.<sup>24</sup> Furthermore, it has been suggested that lithium re-intercalation into the cathode material during discharge is much more hindered than lithium de-intercalation during charge.<sup>38-40,42</sup> In this context, Zheng et al.<sup>40</sup> remarkably showed that overlithiated oxides have a good rate performance during fast charging, while fast discharging alters the material significantly. Assat et al.<sup>43</sup> recently suggested for the  $\text{Li}_2\text{Ru}_{0.75}\text{Sn}_{0.25}\text{O}_3$  model compound that high-voltage charging strongly alters the material and leads to a deterioration of the materials kinetics. Furthermore, they suggested that the reversible anionic oxygen redox causes the slow kinetics and the high resistances.<sup>43</sup> However, there is still a lack of understanding to what extent structural changes on the surface versus in the bulk material might be responsible for those high resistances.

In this study, we will examine the resistance build-up mechanisms of HE-NCM, namely of  $0.42 \text{Li}_2\text{MnO}_3 \cdot 0.58 \text{LiMeO}_2$  ( $\text{Me} = \text{Ni}, \text{Co}, \text{Mn}$ ), using electrochemical impedance spectroscopy (EIS) and power pulse testing over 150 charge-discharge cycles in graphite//HE-NCM full-cells. By using a micro-reference electrode,<sup>44</sup> we can deconvolute the impedance of the anode and the cathode to analyze their individual contributions to the cell impedance obtained by EIS, which we then compare to the resistance obtained via 10 s power pulses. The latter

\*Electrochemical Society Student Member.

\*\*Electrochemical Society Fellow.

<sup>z</sup>E-mail: [tobias-maximilian.teuffl@basf.com](mailto:tobias-maximilian.teuffl@basf.com)

will then be applied to analyze the resistance build-up during cycling, as it is more easily accessible and expeditious for full-cell resistance measurements. We show that the activation of HE-NCM leads to high impedance at low SOCs, which is in line with the findings by other groups.<sup>38,39</sup> We ascribe this phenomenon to the reversible lithiation of an oxygen depleted surface layer, whereby this surface layer is formed upon the activation and cycling of HE-NCM.<sup>24</sup> Furthermore, our data reveal that there is a significant hysteresis between the impedance at low SOC, with a higher impedance during discharge compared to charge at the same SOC. Interestingly, this hysteresis gets more pronounced upon extended charge/discharge cycling and can be correlated to distinct discharge features in  $dQ/dV$  plots. Here, it should be noted that for non-activated HE-NCM there is no hysteresis in the impedance and that the  $dQ/dV$  plot indicates fully-reversible behavior. Finally, we show that the impedance hysteresis at low SOC for activated and cycled HE-NCM increases with increasing upper cutoff potentials and that it disappears once the cells are discharged to 2.0 V. The possible processes which might cause the observed impedance hysteresis and its strong dependence on SOC will be discussed at the end of this work.

### Experimental

**Electrode preparation.**—HE-NCM with the composition  $0.42 \text{ Li}_2\text{MnO}_3 \cdot 0.58 \text{ LiNi}_{0.38}\text{Co}_{0.21}\text{Mn}_{0.41}\text{O}_2$  was obtained from BASF SE (Germany). For coin-cell testing, inks for cathode electrode preparation contained 92.5 wt.% HE-NCM (BASF SE, Germany), 3.5 wt.% polyvinylidene-fluoride binder (PVDF, Solef 5130, Solvay, Belgium), 2 wt.% conductive carbon (Super-C 65, Timcal, Switzerland; BET area of  $\approx 65 \text{ m}^2/\text{g}$ ), and 2 wt.% graphite (SFG6L, Timcal, Switzerland; BET area of  $\approx 17 \text{ m}^2/\text{g}$ ). These materials were dispersed in N-methyl pyrrolidone (NMP, anhydrous, Sigma-Aldrich, USA) and coated onto aluminum foil (16  $\mu\text{m}$ ). Dried electrodes were calendered to a density of  $2.3 \text{ g}/\text{cm}^3$ , resulting in a final electrode thickness of 20  $\mu\text{m}$ . For electrochemical testing, electrodes with 11 mm (for Swagelok T-cells), or 14 mm (for 2032-type coin-cells) were punched out and weighed. The active material loading was  $\approx 6.5 \text{ mg}/\text{cm}^2$ , corresponding to  $\approx 1.6 \text{ mAh}/\text{cm}^2$  (based on a nominal reversible capacity of  $250 \text{ mAh}/\text{g}$ ).

Graphite anodes were commercial electrodes with a graphite loading of  $\approx 6.7 \text{ mg}/\text{cm}^2$ , corresponding to  $\approx 2.4 \text{ mAh}/\text{cm}^2$  (based on a theoretical capacity of  $360 \text{ mAh}/\text{g}$ ). For electrochemical testing, graphite electrodes with a diameter of 11 mm (for Swagelok T-cells), or 15 mm (for 2032-type coin-cells) were punched out. All anode and cathode electrodes were dried overnight under vacuum in an oven within the glovebox ( $\text{O}_2, \text{H}_2\text{O} < 0.1 \text{ ppm}$ , MBraun, Germany) at  $120^\circ\text{C}$  and were not exposed to air after the drying procedure.

**Electrochemical characterization.**—Two different cell setups were used: i) Swagelok T-Cells with a gold-wire micro-reference electrode (GWRE)<sup>44</sup> were used for the EIS measurements and current pulse measurement validation (based on Figure 3), whereby anode and cathode resistances could be determined individually; ii) coin-cells were used for long-term cycling experiments with current pulse measurements, for which the overall full-cell resistance could be determined. 2032-type coin-cells were assembled in an argon filled glovebox using a graphite anode (15 mm diameter), two glass fiber separators (200  $\mu\text{m}$  thickness, VWR, Germany), and a HE-NCM cathode (14 mm diameter). The cells were filled with 95  $\mu\text{L}$  of electrolyte, based on FEC:DEC (12:64 v:v) with 1M  $\text{LiPF}_6$  and 24 %<sub>vol.</sub> of an additional fluorinated co-solvent to improve full-cell cycling stability. Swagelok T-Cells were also assembled in an argon filled glovebox using a graphite anode (11 mm diameter), two glass fiber separators (200  $\mu\text{m}$  thickness, VWR, Germany), and an HE-NCM cathode (11 mm diameter). The cells were filled with 60  $\mu\text{L}$  of the same electrolyte that was used for the coin-cells. Furthermore, the Swagelok T-Cells were equipped with a gold micro-reference electrode (for details see Solchenbach et al.).<sup>44</sup>

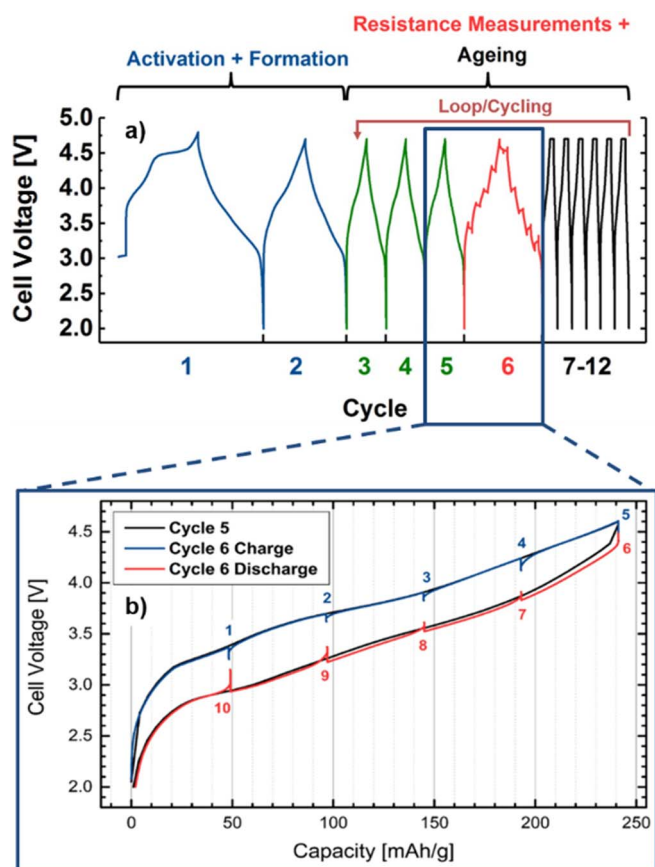


**Figure 1.** a) Graphic representation of the cycling procedure, with the initial cell activation (2.0–4.7 V at 0.067C CC) and cell formation (2.0–4.6 V at 0.1C CC) in blue. The repeat unit for extended cycling consists of 10 cycles: the green lines depict three slow cycles at 0.2C (2.0–4.6 V) at constant current (CC) to adjust the SOC for the resistance measurements at various SOCs in the fourth cycle at 0.2C, shown in red (2.0–4.6 V), followed by six cycles at fast C-rates for cell ageing (2.0–4.6 V) with a charge at 0.5C + 1 h CV and a discharge at 1C. b) Voltage versus capacity plots of cycle 5 and 6, marking the points for the resistance/impedance measurements at 20% SOC intervals during charge and discharge. These data were recorded in CR2032-type coin-cells.

All cells were tested at  $25^\circ\text{C}$  in a temperature-controlled oven (Binder, Germany) using a battery cycler (Series 4000, Maccor, USA). The cycling procedure is depicted in Figure 1a and consisted of the following steps: i) one activation cycle at a C-rate of 0.067C (2.0–4.7 V) and one formation cycle at a C-rate of 0.1C (2.0–4.6 V), shown in blue; ii) the resistance measurement sequence, consisting of 3 cycles at 0.2C (2.0–4.6 V; green lines) to equilibrate the cell to the different C-rate and to set the actual capacity which is used to adjust the different SOC-values during the fourth cycle at 0.2C (2.0–4.6 V; red lines), where EIS and/or pulse current resistance are being obtained; and, iii) 6 fast cycles (black lines) for cell ageing, where the cells were charged/discharged between 2.0–4.6 V with 0.5C (CCCV)/1C (CC), whereby all CV-steps were terminated after 1 h or when the current decreased below 0.01C. The first two cycles (blue lines) were only carried out once, while all other cycle sequences were repeated over the course of extended cycling (as shown in Figure 1). The diagnostic cycles with the resistance measurements were conducted every 10 cycles starting from cycle 6, as shown by the cycling loop in Figure 1a. This means that the resistance was measured after 6, 16, 26, 36, 46 cycles and so on. Note that here all C-rates are referenced to the nominal capacity of the HE-NCM of  $250 \text{ mAh}/\text{g}$  (i.e.,  $1\text{C} \equiv 250 \text{ mA}/\text{g}$  or  $1.6 \text{ mA}/\text{cm}^2$ ).

A typical voltage versus capacity profile is shown in Figure 1b for the cycle at 0.2C just prior to the resistance/impedance

measurements (5<sup>th</sup> cycle, black line) as well as for a cycle during which resistance/impedance measurements are conducted (6<sup>th</sup> cycle; red and blue line). A comparison between these two cycles shows that the resistance/impedance measurements do not influence the overall electrochemical performance. For the example shown in Figure 1b, the resistance measurements were conducted in steps of 20% SOC; for the long-term cycling experiments, they were conducted in steps of 10% SOC, otherwise following the very same procedure. Before the resistance/impedance was measured, the cells were set to rest for 1 h at 25°C, which is reflected by the potential relaxations in Figure 1b.

The resistance was measured by two different approaches at 25°C. One was to conduct electrochemical impedance spectroscopy in galvanostatic mode (GEIS) over a wide frequency range (100 kHz to 60 mHz with an amplitude of 0.9 mA), using a potentiostat (VMP300, BioLogic, France). These experiments were done with Swagelok T-cells equipped with a micro-reference electrode, so that anode and cathode impedances could be determined individually. The other approach was based on current pulse measurements, also referred to as Direct Current Internal Resistance (DCIR),<sup>45</sup> which we conducted either Swagelok T-cell with micro-reference electrode or in coin-cells without reference electrode. DCIR measurements were conducted applying a 10 s long negative current pulse of 0.2C ( $\equiv 0.32 \text{ mA/cm}^2$ ) to the cell after a 1 h rest at OCV (open circuit voltage); the resistance was calculated from the difference between OCV and the potential at the end of the pulse (i.e., after 10 s) divided by the pulse current, as reported elsewhere.<sup>45</sup> To judge the reproducibility of the resistance/impedance data, at least two independent measurements were carried out, and the here presented cycling and resistance/impedance data show the average values, with the error bars reflecting the maximum and minimum of the measured values.

## Results and Discussion

**Measurement and validation of the full-cell resistance by DCIR.**—It has been reported in the literature that overlithiated oxides show drastic increase in resistance upon cycling,<sup>24</sup> which in term might be caused by sluggish kinetics after the activation of the material. Furthermore, it was proposed that charge and discharge follow different pathways and kinetics for lithium extraction and insertion show distinct differences.<sup>38,43</sup> To explore the different contributions to the resistance in graphite//HE-NCM full-cells, we assembled Swagelok T-cells with a micro-reference electrode.<sup>44</sup> This lithiated gold micro-reference electrode allows to differentiate between anode and cathode impedance in a full-cell without disassembling the cell. With this setup, EIS data and current pulse responses were measured after according to the cycling procedure outline in Figure 1 for several SOCs. Figure 2 shows exemplary Nyquist plots for the measurement at 20% SOC during charge for both the cathode (Figure 2b) and the anode (Figure 2c), whereby the red dots represent the measured data and the blue lines are the results from the fitting. The Nyquist plot for the cathode impedance (Figure 2b) shows a high frequency resistance of  $\approx 6 \Omega\text{cm}^2$  as well as two distinct semi-circles, one at high frequencies that has a resistance of  $\approx 4 \Omega\text{cm}^2$  and one at lower frequencies that has a resistance of  $\approx 28 \Omega\text{cm}^2$ . The impedance spectra were fitted with the equivalent circuit model shown in Figure 2a, whereby the high frequency resistance is described by a simple resistor ( $R_{\text{HFR}}$ ) and the two semi-circles were fitted with two R/Q elements (R = resistor, Q = constant phase element). Note that when using the micro-reference electrode,  $R_{\text{HFR}}$  of the cell is split into two essentially equal HFR contributions from the anode ( $R_{\text{HFR,anode}}$ ) and cathode ( $R_{\text{HFR,cathode}}$ ).<sup>44</sup> Previous studies have shown that the first semi-circle of the cathode impedance ( $R_1/Q_1$ ) shows up at high frequencies ( $>5 \text{ kHz}$ ) and can be assigned to a contact resistance at the interface of the cathode electrode with the aluminum current collector.<sup>24,46–48</sup> This can be rationalized by considering the electrode capacitance corresponding to this first semi-circle:

$$C_1 = \frac{1}{R_1 2 \pi f_{\text{max}}} \quad [1]$$

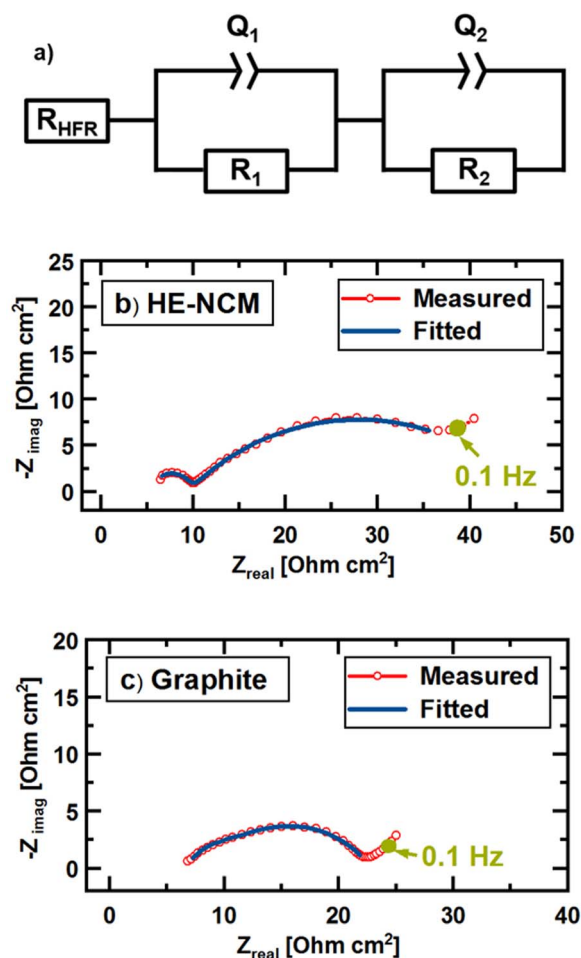


**Figure 2.** a) Equivalent circuit model for the fitting of the anode and the cathode impedance spectra. Exemplary Nyquist plots obtained from a graphite//HE-NCM full-cell with a micro-reference electrode<sup>44</sup> at 20% SOC during charge (for cycle 6 in Figure 1) are shown for individually for: b) the cathode and c) the anode. The measured data are shown by the red dots and the fitted data are represented by blue lines, while the green dots mark the impedance at 0.1 Hz. Galvanostatic impedance spectra were measured at 25°C from 100 kHz to 60 mHz with an amplitude of 0.9 mA.

where  $C_1$  is the capacitance (approximated from the constant phase element  $Q_1$ ),  $R_1$  is the diameter of the semi-circle, and  $f_{\text{max}}$  is the frequency corresponding to the apex of the first semi-circle. For the data shown in Figure 2b, the resistance is  $R_1 \approx 4 \Omega$  and  $f_{\text{max}} \approx 31 \text{ kHz}$ , equating to an electrode capacitance of  $\approx 1 \mu\text{F}$ . To examine its origin, the capacitance can be normalized either to the geometric surface area of the aluminum current collector ( $\approx 0.95 \text{ cm}^2$ ) or to the surface area of the cathode electrode ( $\approx 450 \text{ cm}^2$ , based on mass and BET surface area of the HE-NCM and the conductive carbons within the electrode). This equates to normalized capacitances of either  $\approx 1.1 \mu\text{F/cm}^2$  or  $\approx 0.002 \mu\text{F/cm}^2$ . Comparing these to a typical double-layer capacitance, which is in the order of  $\approx 10^1 \mu\text{F/cm}^2$ ,<sup>49</sup> it is clear that the first semi-circle must correspond to a contact resistance at the interface between the cathode electrode and the current collector ( $R_{\text{contact}}$ ). Detailed analysis onto the origin of these contact resistance can be found elsewhere.<sup>46–48</sup> The second somewhat depressed semi-circle of the cathode impedance ( $R_2/Q_2$ ), occurring in the lower frequency region, can be assigned to the charge-transfer resistance of the cathode ( $R_{\text{CT,cathode}}$ ). Thus, the cathode impedance can be defined as:

$$R_{\text{cathode}} = R_{\text{HFR,cathode}} + R_{\text{contact,cathode}} + R_{\text{CT,cathode}} \quad [2]$$

The Nyquist spectra of the anode impedance (Figure 2c) shows a high frequency resistance of  $R_{\text{HFR,anode}} \approx 7 \Omega\text{cm}^2$  and a superposition

of two semi-circles with a total diameter of  $\approx 15 \Omega\text{cm}^2$ , which was fitted with the same equivalent circuit model (Figure 2a), containing two R/Q elements. The first R/Q element ( $R_1/Q_1$ ) can be assigned to the SEI resistance/capacitance and the second R/Q element ( $R_2/Q_2$ ) describes the charge-transfer resistance. Thus, the anode impedance can be defined as:

$$R_{\text{anode}} = R_{\text{HFR,anode}} + R_{\text{SEI,anode}} + R_{\text{CT,anode}} \quad [3]$$

Furthermore, the full-cell resistance can then be defined as the sum of anode and cathode resistance:

$$R_{\text{cell}} = R_{\text{cathode}} + R_{\text{anode}} \quad [4]$$

Simple current pulses are often used in order to have an easy and fast method to determine the cell resistance and the resistance build-up;<sup>36,38</sup> this method is also referred to as DCIR method (Direct Current Internal Resistance).<sup>45</sup> As the response to current pulses is strongly dependent on the current and the pulse duration, we carefully chose the duration and the current of the pulse in order to minimize changes of the SOC and to receive results that are comparable to the low frequency resistance obtained by EIS measurements. Therefore, the pulse was applied from OCV always with a negative current (i.e., a discharge current) of 0.2C for a duration of 10 s, corresponding to a change in SOC of 0.06%, which we consider to be negligible. From the difference between OCV and the voltage at the end of the pulse (i.e., at 10 s) and the pulse current, the effective resistance was calculated using Ohm's law (for details see reference<sup>45</sup>). To quantify the resistance contributions from anode and cathode, we conducted the DCIR measurements in the same Swagelok T-cell setup with micro-reference electrode that was used for the EIS measurements. Please note that at each SOC, the cell was rested at OCV for 1 h before the 10 s current pulse was applied, followed by a 5 min rest before the impedance measurements were carried out. With this sequence, we expect that the EIS results are not influenced by the DCIR measurements or vice versa. To differentiate between the low frequency resistance obtained by EIS measurements and the DCIR, we will refer to the latter as area specific resistance (ASR, referenced to the geometric surface area). The ASRs measured in the Swagelok T-cells with micro-reference electrode are defined as follows:

$$\text{ASR}_{\text{cell}} = \text{ASR}_{\text{cathode}} + \text{ASR}_{\text{anode}} \quad [5]$$

As the resistances obtained from the DCIR measurements are strongly dependent on time and duration of the current pulse, its value needs to be compared to full EIS measurements in order to understand its physical meaning. Therefore, Figure 3 compares the results from the fitted impedance spectra (EIS, blue lines) with the resistances measured by the DCIR method with 0.2C discharge current pulses for 10 s (DCIR, green lines). Figures 3a–3c depict the anode, cathode, and full-cell resistances versus SOC as the cell is either being charged (square symbols) or being discharged (triangular symbols), whereby the EIS data correspond to the sum of  $R_{\text{HFR}} + R_1 + R_2$  shown in Figure 2a (referred to further on as low frequency resistance) and the DCIR data are the resistance calculated from the 10 s pulse (always a discharge pulse). These resistances are plotted versus the capacity (every  $\Delta 20\%$  SOC), starting at  $\approx 47 \text{ mAh/g}$  ( $\equiv 20\%$  SOC) up to  $\approx 235 \text{ mAh/g}$  ( $\equiv 100\%$  SOC for an upper limit of 4.6 V). The EIS based low frequency resistances of the graphite anode (blue symbols/lines in Figure 3a) are roughly constant ( $\approx 22\text{--}24 \Omega\text{cm}^2$ ) and independent of whether the cell is being charged or being discharged. The latter behavior is also observed for the DCIR-values of the anode (green symbols/lines in Figure 3a), even though its values ( $\approx 29\text{--}31 \Omega\text{cm}^2$ ) are  $\approx 20\%$  higher than the EIS derived resistances. The higher values measured by DCIR can be explained by a visual comparison with Figure 2c, where the green spot marks the EIS data point at 0.1 Hz, which is the approximately equivalent nominal frequency corresponding to a 10 s pulse: its real-axis value is  $\approx 15\%$  higher than the low frequency resistance from the EIS fitting (i.e.,  $\approx 25 \Omega\text{cm}^2$  versus  $\approx 22 \Omega\text{cm}^2$ ), reasonably consistent with the  $\approx 20\%$  higher 10 s DCIR value.

In contrast to the anode resistances, EIS and DCIR results for the cathode (Figure 3b) show a strong SOC dependent behavior and sub-

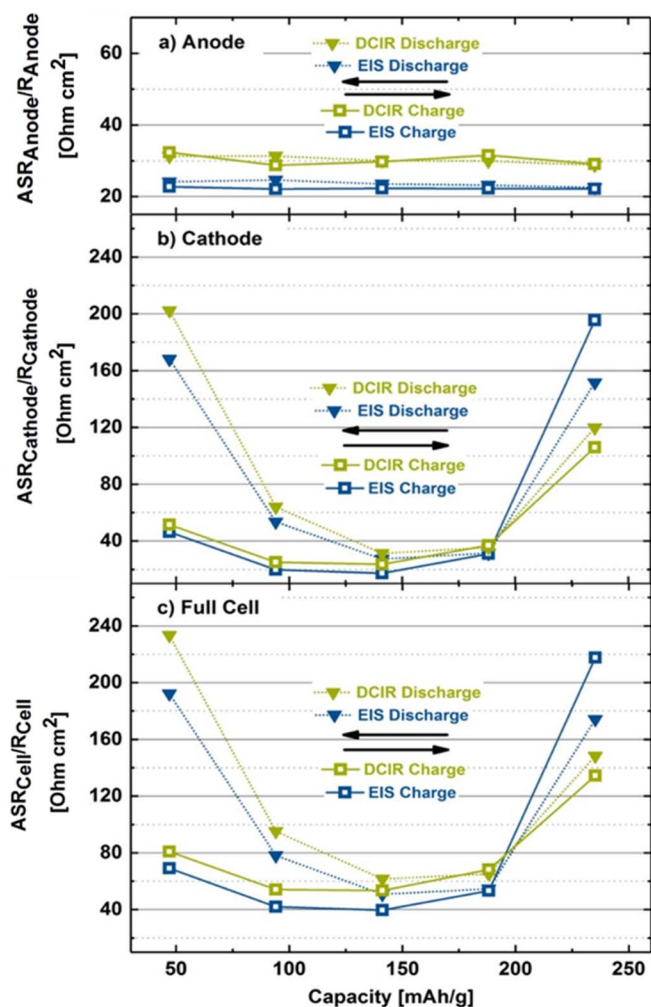


**Figure 3.** Resistances vs. SOC during the charge and the discharge pathway of a graphite/HE-NCM cell at 0.2C and 25°C (for cycle 6, see Figure 1), obtained from the EIS-based low frequency resistance (blue symbols/lines) and from discharge current pulses (DCIR; green symbols/lines), using a Swagelok T-cell with a micro-reference electrode. Impedance spectra were evaluated with the equivalent circuit shown in Figure 2a, while DCIR values were calculated by Ohm's law. a) Anode resistances; b) cathode resistances; and, c) full-cell resistances. The DCIR values were determined from 10 s long 0.2C discharge current pulses; impedance spectra were recorded from 100 kHz to 60 mHz with an amplitude of 0.9 mA. After charge/discharge to a certain SOC, the cell was held at OCV for 1 h before the DCIR was measured, followed by another 5 min at OCV before recording EIS data.

stantial differences between the charge (square symbols) and the discharge (triangular symbols) pathway (note: charge/discharge pathway refers to whether the cell is being charged/discharged; the pulse is always a discharge pulse). At first, we want to focus on the comparison between the resistance values based on the low frequency EIS resistance (blue symbols/lines in Figure 3b) and the DCIR values (green symbols/lines in Figure 3b). Again, the former are generally lower than the latter, which we ascribe to the same effect as discussed above, namely that the real part of the resistance at 0.1 Hz (see green dot in Figure 2b) is higher than the low frequency resistance. One exception is the resistance at 235 mAh/g ( $\equiv 100\%$  SOC for an upper limit of 4.6 V), for which the EIS derived value is higher (Figure 3b); furthermore, while the EIS based resistance at 235 mAh/g should be the same for the charge and the discharge pathway, it is  $\approx 20\%$  higher for the former, even though these measurements are only separated by a 1 h OCV phase. To explain these differences, it is noted that in contrast to all other cathode EIS data, the Nyquist spectra at 235 mAh/g ( $\equiv 100\%$

SOC) do not show the shape of a semi-circle (data not shown), but show a blocking electrode behavior, analogous to what can be observed for an LNMO cathode ( $\text{LiNi}_{0.5}\text{Mn}_{1.5}\text{O}_4$ ),<sup>47</sup> for which all lithium can be fully extracted at 100% SOC, as is the case for the HE-NCM material. In that case, the charge-transfer reaction is hindered and capacitive coupling becomes the main process during the impedance measurement, as was shown by Landesfeind et al.<sup>47</sup> for a fully delithiated LNMO cathode, for which nearly perfect blocking conditions were obtained. Due to this phenomenon, namely that the EIS response of a fully delithiated cathode active material is dominated by capacitive coupling, the charge-transfer resistances obtained by fitting EIS data at 100% SOC generally show large and unreliable values, explaining the discrepancy for the two EIS measurements at 235 mAh/g in Figure 3b. As this phenomenon does not occur for discharge pulse measurements, we expect that the DCIR-based values for the cathode resistance at 235 mAh/g ( $\equiv$  100% SOC) are accurate and more reliable than the EIS-based values.

Finally, Figure 3c shows the full-cell resistance based on EIS (blue symbols/lines) and DCIR (green symbols/lines) measurements, which of course are simply the summation of the anode and cathode impedance. Comparing the anode and cathode contribution of the full-cell resistance (Figure 3), it is obvious that the SOC dependency and the hysteresis between the charge and the discharge pathway is caused by the cathode, while the anode only adds a more minor linear offset to the full-cell resistance. Owing to the reasonably good correlation between the EIS- and DCIR-based resistances as well as the simply linear offset and the overall minor contribution of the anode (particularly at low and high SOC), the SOC dependence of the HE-NCM resistance and its hysteresis are largely reflected by the full-cell DCIR resistances. Owing to the simplicity of full-cell DCIR measurements, requiring no reference electrode and no EIS measurements, we will now use the full-cell DCIR resistances (based on 0.2C discharge pulses over 10 s) to further investigate the unusual SOC dependence of the resistance and its hysteresis of HE-NCM cathode active materials cycled in graphite//HE-NCM full-cells. Here it should be noted that our study does not focus on the absolute resistance values, i.e., that the scope of this work is not to quantify absolute impedance build-up values, but that we rather want to characterize the charge/discharge pathway dependence of HE-NCM cathode active materials. In our opinion, the full-cell current pulse based DCIR method offers a reliable and quick access to the approximate cathode area specific resistance (ASR) for the practical and well-proven coin-cell design for long-term cycling studies.

**Structural changes due to high voltage activation.**—Figure 4a depicts the cycling stability of graphite//HE-NCM full-cells (coin-cells) cycled up to 4.1 V (red symbols/line, continuously cycled to 4.1 V) and cells cycled up to 4.7 V for the first-cycle activation process (black symbols/line, with subsequent cycles only up to 4.6 V). Cells cycled between 2.0 V and 4.1 V show a very good cycling stability, but since the HE-NCM was not activated, only very little capacity can be extracted from the cell ( $<100$  mAh/g). In contrast, when HE-NCM is activated (i.e., cycled beyond the potential plateau at 4.5 V in the first cycle), a tremendous increase in the specific capacity of HE-NCM to  $\approx 250$  mAh/g is observed. Nonetheless, the cycling performance of the material deteriorates rather quickly, which can be explained by several mechanisms triggered by the cycling to high voltages, like oxygen release from the surface-near regions,<sup>21,23,24</sup> irreversible transition metal migration,<sup>18,28,35</sup> and anionic redox in the bulk.<sup>26–28,43</sup> After every 6 fast 0.5C/1C cycles, 4 diagnostic cycles with a charge and discharge rate of 0.2C were applied (corresponding to the procedure shown in Figure 1). From Figure 4a it can be seen that the discharge capacity for the slow (0.2C) and the fast discharge rate (1C) are essentially the same, pointing towards a continuous capacity loss caused by loss of active lithium or by loss of active cathode material due to side reactions.<sup>24</sup> However, Figure 4a clearly points out that cycling to high voltages (e.g. 2.0–4.6 V in a full-cell) is required in order to achieve high capacities that make the material interesting for commercial ap-

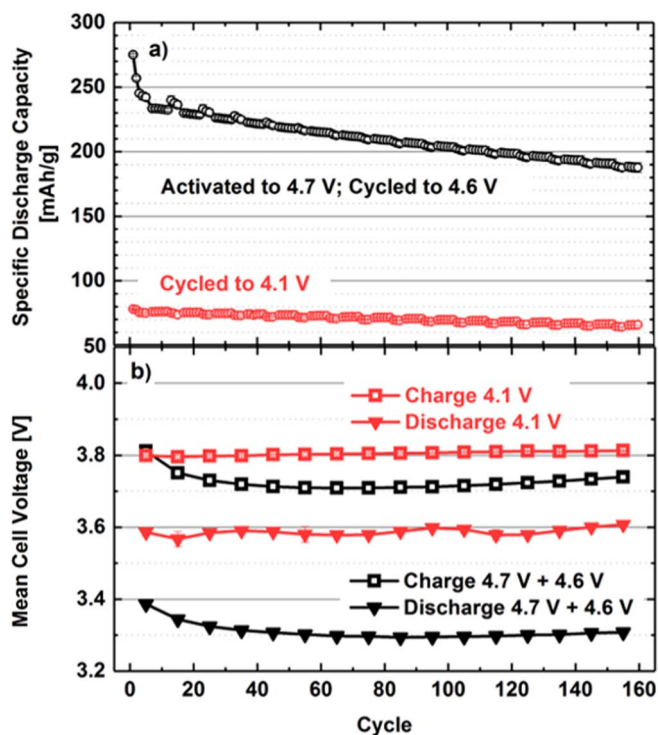


**Figure 4.** Electrochemical cycling of graphite//HE-NCM full-cells (coin-cells) at 25°C according to the procedure shown in Figure 1. Cells with activated HE-NCM (one cycle to 4.7 V) are shown in black and were cycled between 2.0–4.6 V (initial activation cycle between 2.0–4.7 V), cells with non-activated HE-NCM are shown in red and were cycled between 2.0–4.1 V. Full-cell resistances were measured every 10 cycles by the DCIR method in 10% SOC intervals during charge and discharge. a) Specific discharge capacities for cells with activated (black) and non-activated (red) HE-NCM; b) corresponding charge-averaged mean cell voltages at 0.2C (for CC charge/discharge). For the determination of the mean voltage, the last 0.2C cycle of each sequence (Figure 1a) was used; e.g. cycle 5, 15, 25, and so on. The mean cell voltage was calculated as defined by Jung et al.<sup>9</sup>  $\bar{V}_{\text{charge/discharge}} = \int V_{\text{charge/discharge}} \cdot dQ_{\text{charge/discharge}} / \int dQ_{\text{charge/discharge}}$ .

plications and one has to deal with the structural drawbacks that are associated with the high-voltage activation.

The charge-averaged voltage (square symbols) and discharge (triangular symbols) voltages for the 0.2C cycles (the last of each 0.2C shown in Figure 1a, prior to the DCIR measurements; e.g., cycle 5, 15, 25 and so on) are shown in Figure 4b, indicating that the cells with non-activated HE-NCM cycled between 2.0 V and 4.1 V show no voltage fading and a voltage-hysteresis of only  $\approx 200$  mV (here defined as the difference between the mean charge and discharge voltage). On the other hand, the cells with activated HE-NCM cycled between 2.0 V and 4.6 V show a much larger voltage-hysteresis of  $\approx 400$  mV, in addition to a substantial voltage-fading over 160 cycles of  $\approx 180$  mV in the mean discharge voltage and  $\approx 160$  mV in the mean charge voltage (see Figure 4b). This points towards a major transformation of the bulk HE-NCM material, a phenomenon which has been examined by many different groups and has been ascribed to transition metal migration within the bulk material for both lithium- and manganese-rich HE-NCM<sup>18,35</sup> as well as for related lithium-rich materials.<sup>33</sup> It has been suggested that the charge/discharge voltage-hysteresis might be correlated to reversible transition metal migration between the lithium and the transition metal layer,<sup>18,35,50</sup> while recent studies showed that transition metal migration also correlates with the reversible anionic oxygen redox within the bulk material.<sup>27,28</sup> Furthermore, it was suggested that reversible transition metal movement might occasionally result in an irreversible trapping of the transition metals in the lithium layer,<sup>18,35</sup> causing bulk material changes which lead to voltage fading.<sup>18,19,33,35</sup>

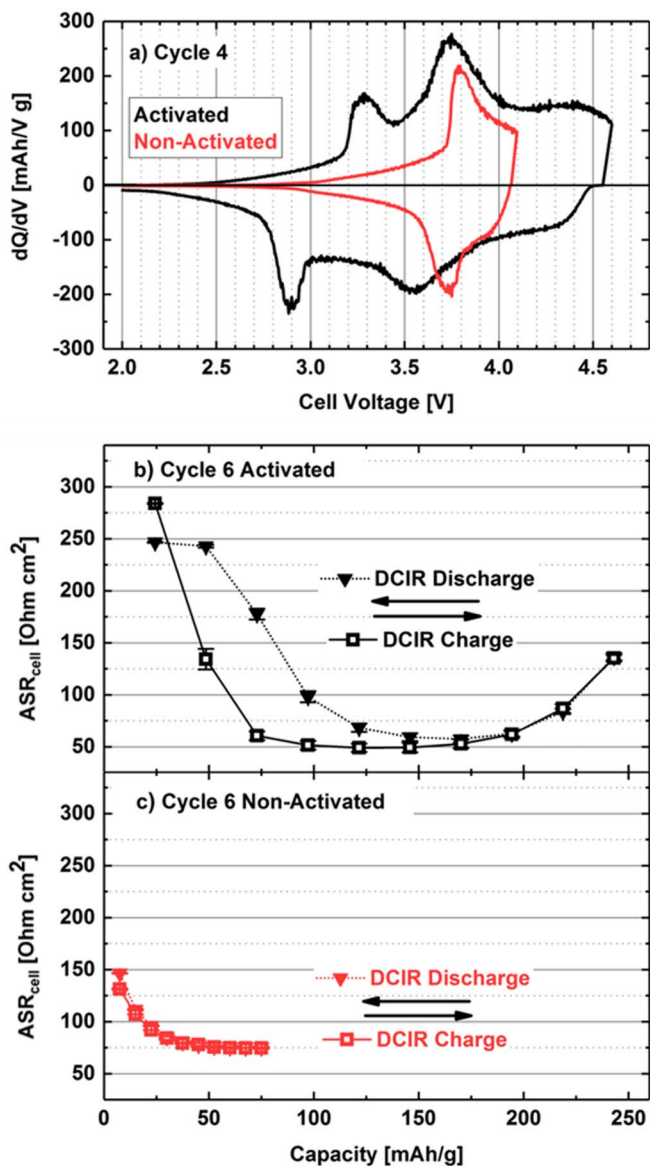


**Figure 5.** a) Full-cell  $dQ/dV$  of cycle 4 at 0.2C (taken from the data set of Figure 4) for cells with activated (black) and non-activated (red) HE-NCM at 25°C. The corresponding full-cell DCIR-based resistances (10 s long 0.2C discharge pulses at 25°C) from cycle 6 are shown for b) the activated, and c) the non-activated HE-NCM. DCIR measurements were conducted in 10% SOC intervals, always following a 1h OCV period.

Further differences between cells with non-activated HE-NCM cycled up to 4.1 V (red line) and with activated HE-NCM (first cycle to 4.7 V) cycled up to 4.6 V (black line) can be seen in Figure 5a, showing the differential capacity curves for the fourth cycle at 0.2C. The potentials that were recorded with the reference electrode during the initial cycles (data not shown) show that the full-cell  $dQ/dV$  is not strongly affected by the graphite anode and reflects the behavior of the HE-NCM cathode; the behavior of the  $dQ/dV$  is also in line with half-cell data reported in earlier studies using the exact same material.<sup>23,24,35</sup> Clearly, for non-activated HE-NCM, a fully reversible behavior without voltage-hysteresis is observed (with charge/discharge peaks at  $\approx 3.8/3.7$  V), contrary to the large voltage-hysteresis in the drastically different differential capacity curves of activated HE-NCM. The first distinct difference is the appearance of a charge peak at already  $\approx 3.3$  V for the activated HE-NCM, which in a previous study we showed to be due to an oxygen depleted surface layer produced by the lattice oxygen release from the near-surface layer of the HE-NCM particles.<sup>24</sup> We pre-

viously showed by careful quantification of the capacity contribution of this first charge peak that it represents a reversible rocksalt-to-spinel transformation upon delithiation.<sup>24,51,52</sup> This surface layer appeared in HRTEM images as cation disordered surface phase and was referred to as  $M'_3O_4$  spinel type layer, as TEM did not allow to distinguish between the two phases (due to the poor electron density of Li).<sup>24</sup> From the careful quantification shown by Teufl et al.,<sup>24</sup> we expect that this surface layer is electrochemically active and thus can reversibly transform between spinel and rocksalt during cycling. As mentioned above we expect a disordered  $M'_3O_4$  spinel type surface layer, while the term rocksalt refers to the overlithiated stoichiometry of this  $M'_3O_4$  surface layer. The existence of such an overlithiated disordered spinel phase (referred to as rocksalt phase) suggests that the lithium content of this surface layer differs substantially between the charged and the discharged state (delithiation expected around 3.3 V), which can be rationalized by the capacity contribution of this surface layer, as shown in a previous study.<sup>24</sup> In this study we therefore refer to it as oxygen depleted surface layer and suggest it to have a rocksalt like structure at low SOCs and a spinel type structure above 3.3 V. A further  $dQ/dV$  characteristic of activated HE-NCM seen in Figure 5a is the disappearance of the discharge peak at  $\approx 3.7$  V, which is reversible for non-activated HE-NCM, concomitant with the occurrence of a new discharge peak at a  $\approx 1$  V lower potential (i.e., at  $\approx 2.9$  V). This  $\approx 1$  V hysteresis was already noted by Croy et al.,<sup>50</sup> and can be rationalized by reversible transition metal migration and reversible oxygen redox in the bulk of the HE-NCM material.<sup>18,28,35</sup>

The full-cell DCIR measurements taken during cycle 6 of the data set shown in Figure 4 (in 10% SOC intervals, according to the procedure depicted in Figure 1) can be seen in Figure 5b for the activated and in Figure 5c for the non-activated HE-NCM. The latter shows resistances which are identical along the charge and discharge pathway, as expected for traditional layered oxides, with a value of  $\approx 70 \Omega\text{cm}^2$  over a wide range; only at very low SOCs (i.e., at  $<25$  mAh/g, corresponding to  $<40\%$  SOC for the non-activated HE-NCM), the resistance increases up to  $\approx 150 \Omega\text{cm}^2$ , which can be rationalized by the lower lithium mobility in nearly fully lithiated layered oxides.<sup>53-55</sup> A strikingly different behavior is observed for the cells with activated HE-NCM (Figure 5b): Upon charging (open squares), very high resistances of  $\approx 280 \Omega\text{cm}^2$  are obtained at  $\approx 25$  mAh/g ( $\equiv 10\%$  SOC), which rapidly decrease to a minimum of  $\approx 50 \Omega\text{cm}^2$  at around 120 mAh/g ( $\equiv 50\%$  SOC), followed by a gradual increase to  $\approx 135 \Omega\text{cm}^2$  by the end-of-charge along the charge pathway (i.e., at 245 mAh/g,  $\equiv 100\%$  SOC), which is in line with the behavior reported in the literature.<sup>38,39</sup> Even more interesting is the behavior during discharge of the activated HE-NCM (filled triangles), which first follows the resistance observed along the charge pathway down to 145 mAh/g ( $\equiv 60\%$  SOC), but upon further discharge becomes much larger than that measured along the charge pathway. For example, the resistance at  $\approx 45$  mAh/g ( $\equiv 20\%$  SOC) along the discharge pathway is  $\approx 240 \Omega\text{cm}^2$ , much higher than the  $\approx 135 \Omega\text{cm}^2$  obtained along the charge pathway at the same SOC, clearly indicating a higher energy barrier for lithium intercalation into the HE-NCM material. After discharging the cell down to  $\approx 25$  mAh/g ( $\equiv 10\%$  SOC), this resistance hysteresis diminishes again.

Our interpretation of the observed resistance hysteresis is as follows: We believe that the rapid resistance drop along the charge pathway (open squares Figure 5b) from 25 mAh/g ( $\equiv 10\%$  SOC;  $\approx 3.1$  V) to 45 mAh/g ( $\equiv 20\%$  SOC;  $\approx 3.3$  V) is caused by the rocksalt-to-spinel transformation of the oxygen depleted surface layer formed on the HE-NCM particles by lattice oxygen release during activation and subsequent cycling;<sup>24</sup> upon its delithiation, this surface layer changes from a poorly lithium ion conducting rocksalt to a well conducting spinel.<sup>51,52</sup> This surface layer was shown to be delithiated during charge in the potential range between  $\approx 3.0$ – $3.5$  V.<sup>24</sup> During discharge, the surface layer will relithiate and back-transform into a rocksalt structure, which will lead again to the very high resistance observed towards the end of the discharge. With regards to the large resistance hysteresis at low SOC, we expect that during discharge in the range from 145 mAh/g ( $\equiv 50\%$  SOC) to 45 mAh/g ( $\equiv 20\%$  SOC), the

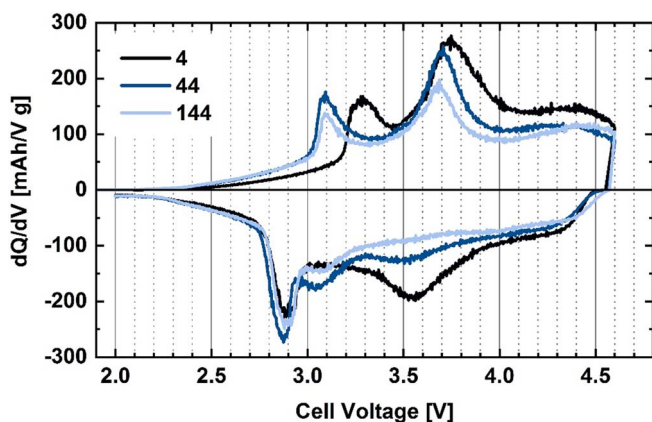


**Figure 6.** Full-cell dQ/dV of cycle 4 (black line), cycle 44 (dark blue line) and cycle 144 (light blue line) measured at 0.2C for cells with activated HE-NCM at 25°C (taken from the data set of Figure 4).

discharge resistance is strongly affected by the extent of reversible and irreversible migration of transition metals that occupy the lithium diffusion paths. The resistance hysteresis would then be related to a hysteresis in the extent of transition metal occupation in the lithium layer, which within a given charge/discharge cycle would have to correspond to a hysteresis in the reversible occupation of the transition metals in the lithium layer, as will be discussed in detail later on.

Ongoing structural changes during the first 144 cycles can be seen in the dQ/dV plots in Figure 6, where several differences can be noted, particularly between cycle 4 and cycle 44. Comparing the first charge peak of cycle 4 (Figure 6; black line) to cycle 44 (Figure 6; dark blue line) and cycle 144 (Figure 6; light blue line), it is apparent that this peak changes mostly during the initial cycles, where the surface restructuring mainly takes place. It has been reported that the surface restructuring after oxygen release occurs during the first 25 cycles, which is in good accordance with this peak shifting from  $\approx 3.3$  V to  $\approx 3.1$  V during the first 44 cycles, with little further changes up to 144 cycles. Furthermore, increasing hysteresis and voltage-fading can be seen during discharge, especially for the peak at  $\approx 3.5$  V during discharge that is present in cycle 4 and has disappeared after 44 cycles. In summary, the major transformations occur during the initial cycles and only minor differences can be seen between cycle 44 and cycle 144 in Figure 6. This is in good accordance with the voltage characteristics of the activated HE-NCM shown in Figure 4b, where the main part of the voltage-fading is shown to occur during the first 50 cycles. As the major structural changes already occur during the initial cycles (Figure 4b and Figure 6), we conducted the further analysis of the resistance behavior during cycle 46 where the extent of capacity fading is still low ( $\approx 240$  mAh/g for cycle 6 and  $\approx 225$  mAh/g for cycle 46; see Figure 4a).

**Influence of the upper cutoff on the reversibility of the resistance.**—As shown in Figure 5, charge/discharge pathway dependency of the resistance is obtained for cells with activated HE-NCM cycled between 2.0 V and 4.6 V (after first-cycle activation to 4.7 V), which is definitely not visible for cells with non-activated HE-NCM cycled only up to 4.1 V. In order to determine the point from which the resistance hysteresis starts to occur for cells with activated HE-NCM (at 4.7 V in the first cycle), the cells were cycled between 2.0 V and 4.6 V according to the procedure shown in Figure 1, except that the maximum SOC value of the diagnostic cycle during which the DCIR-values are measured (see red cycle in Figure 1) was modified as follows: a first diagnostic cycle was done from 0% SOC (2.0 V) to 40% SOC and back to 0% SOC (2.0 V), recording the DCIR at 10% SOC intervals (100% SOC being defined at 4.6 V, corresponding to  $\approx 225$  mAh/g); this was followed by a subsequent diagnostic cycle from 0-60-0% SOC, then from 0-80-0% SOC, and finally from 0-100-0% SOC. For simplicity, these four diagnostic cycles were

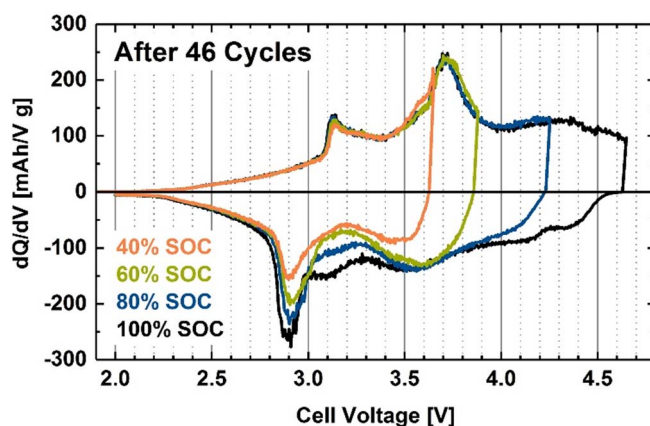


**Figure 7.** Full-cell dQ/dV of activated HE-NCM (at 4.7 V in the first cycle) at 0.2C after 46 cycles between 2.0–4.6 V according to the procedure shown in Figure 1, except that the upper charge cutoff in the DCIR measurement cycle (red cycle in Figure 1) was modified as follows: in a first cycle it the upper SOC was increased to 40% (orange), in a second cycle, to 60% SOC (green), in a third cycle to 80% SOC (blue), and in a fourth cycle to 100% (black), with 100% SOC being defined by the  $\approx 225$  mAh/g obtained for cycling at 0.2C between 2.0–4.6 V.

counted as one cycle and they were carried out each tenth cycle. The results for this sequence after 46 cycles are shown in Figure 7 and Figure 8.

The resistances measured during charge (open squares) and discharge (closed triangles) for cells with activated HE-NCM charged to different SOC after 46 cycles are shown in Figure 8, and the corresponding dQ/dV plots are shown in Figure 7, both for cases where the cells are charged/discharged to 40% SOC (orange), 60% SOC (green), 80% SOC (blue) and 100% SOC ( $\equiv 4.6$  V, black). Figure 8a shows the resistance for a charge up to only 40% SOC (corresponding to  $\approx 90$  mAh/g obtained at  $\approx 3.7$  V) followed by a complete discharge to 2.0 V, illustrating that only a negligible difference in resistance between charge/discharge pathways is observed. However, upon increasing the upper cutoff potential by charging the cell to 60% SOC ( $\approx 135$  mAh/g obtained at  $\approx 3.9$  V, Figure 8b), 80% SOC ( $\approx 180$  mAh/g obtained at  $\approx 4.3$  V, Figure 8c), and finally 100% SOC ( $\approx 225$  mAh/g obtained at  $\approx 4.6$  V, Figure 8d), it becomes obvious that the resistance hysteresis between charge and discharge pathways develops and substantially grows with increasing SOC.

Comparison with the dQ/dV plots from Figure 7 now allows to draw a correlation between the pathway dependence of the resistances and the electrochemical characteristics of the activated HE-NCM. From Figure 7 it can be clearly seen that the capacity charged in the high voltage region ( $>4.0$  V) can only be regained during discharge at potentials below 3.0 V, so that this high irreversibility in the dQ/dV plot of  $\approx 1$  V, also reported in the literature<sup>50</sup> mirrors the above observed resistance hysteresis. It has been shown that with increasing SOC also the voltage hysteresis between charge and discharge increases, suggesting this must be caused by concomitant changes in the bulk of the HE-NCM material.<sup>56</sup> For a related lithium-rich layered oxide, Assat et al.<sup>43</sup> recently suggested that high voltage charging would lead to oxygen anionic redox, which on one hand enables high capacities, but owing to its slow kinetics also leads to voltage hysteresis and high impedances. Later on, Gent et al.<sup>28</sup> also provide evidence that the oxygen anionic redox is coupled intimately with reversible transition metal migration. The latter, we believe, is reflected in the here observed charge/discharge pathway dependence of the resistance, which only develops at high SOC ( $>40\%$ , see Figure 8).

**Transition metal migration and its influence on the resistance.**—Transition metal migration in lithium-rich layered oxides is a well-known phenomenon and has been the object of numerous studies. It has been shown that reversible and irreversible transition metal

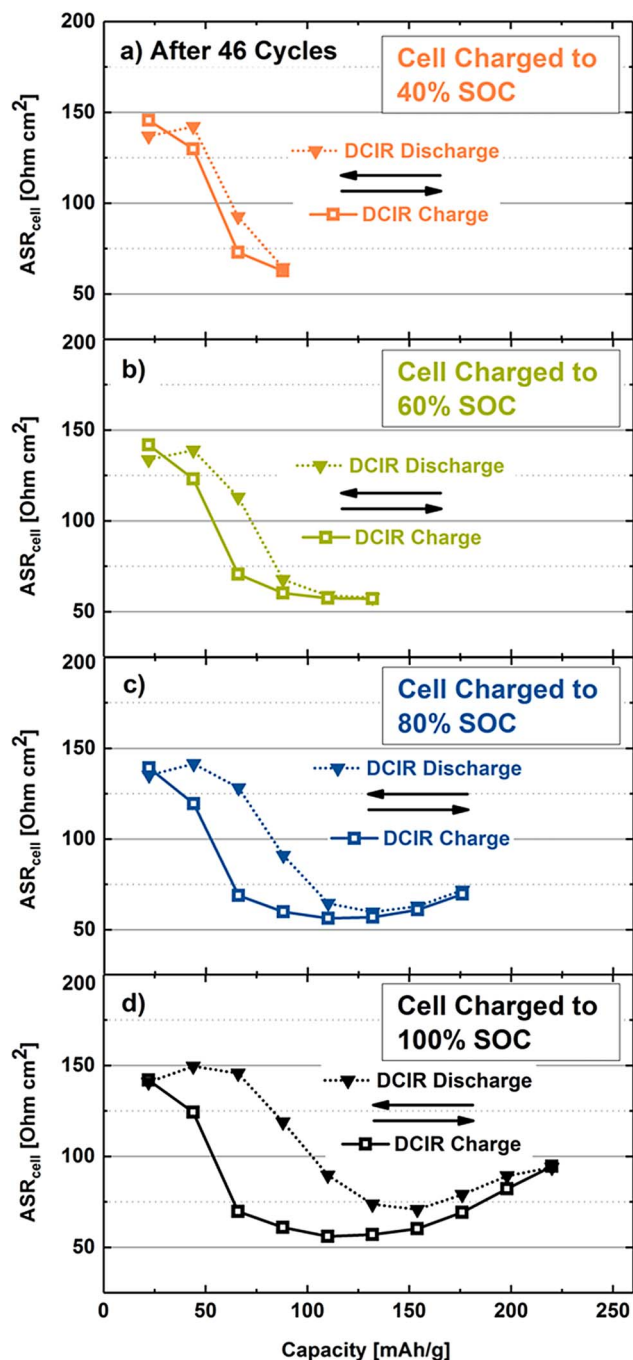
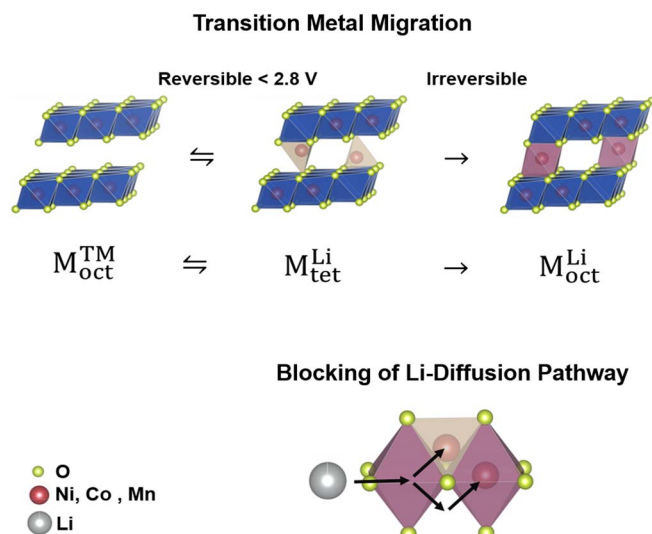


**Figure 8.** Full-cell resistances of activated HE-NCM (at 4.7 V in the first cycle) obtained by DCIR (10 s long 0.2C discharge pulses at 25°C) for different upper cutoff SOC-values during four DCIR measurement cycles, corresponding to the dQ/dVs shown in Figure 7. Prior to taking the here shown DCIR-based resistances at 10% SOC intervals, the cells were cycled for 46 cycles between 2.0 and 4.6 V according to Figure 1 and then cycled between 0% SOC (at 2.0 V) and different upper SOC values of: a) first 40% SOC, b) then 60% SOC, c) then 80% SOC, and, d) finally 100% SOC (4.6 V), whereby 100% SOC correspond to the  $\approx 225$  mAh/g obtained for cycling at 0.2C between 2.0–4.6 V.

migration, even if the fraction of migrated transition metals is fairly small, has a detrimental effect on actual cell performance of these materials;<sup>18,29,32,33,35,57</sup> on the other hand, however, it has also been suggested that transition metal migration might be the reason why HE-NCMs can be cycled reversibly to 100% SOC (referenced to the lithium in the lithium layer).<sup>28,35</sup> Based on these studies, our cell resis-



**Scheme 1.** Upper part: schematic illustration of the transition metal and the lithium layers, depicting the suggested reversible transition metal migration into tetrahedral positions in the lithium layer ( $M_{tet}^{Li}$ ) and irreversible migration into octahedral positions in the lithium layer ( $M_{oct}^{Li}$ ) during cycling, as shown by Kleiner et al.<sup>35</sup> Lower part: retarding effect of migrated transition metals (marked by red spheres for both tetrahedral and octahedral sites in the lithium layer) on lithium diffusion within lithium-rich layered oxide materials.

tance measurements in Figure 8 thus indicate that at high degrees of delithiation (i.e., at high SOC) transition metals are prone to migrate reversibly into thermodynamically favorable positions, proposed to be the tetrahedral and octahedral sites in the lithium layer.<sup>35</sup> Scheme 1 depicts our current view of the bulk transition metal movements between the layers, suggesting that during delithiation transition metals first migrate into tetrahedral positions of the lithium layer ( $M_{tet}^{Li}$ , see upper panel in Scheme 1),<sup>18,35</sup> a process which was suggested to be almost entirely reversible.<sup>28,35</sup> Kleiner et al.<sup>35</sup> recently hypothesized that over the course of cycling, transition metals might also occasionally further migrate into octahedral positions in the lithium layer ( $M_{oct}^{Li}$ ), deduced from long-term powder diffraction data which showed that the transition metal occupancy of octahedral sites in the lithium layer is independent of SOC and increases upon cycling, viz., from  $M_{oct}^{Li} \approx 2\%$  after the first activation cycle to  $M_{oct}^{Li} \approx 5\%$  after 100 cycles. Furthermore, these authors showed that transition metals in tetrahedral positions of the lithium layer occur exclusively in the charged state (i.e., at high SOC) and that tetrahedral migration is reversible during discharge, with the fraction of transition metals moving reversibly into tetrahedral sites remaining essentially constant over cycling ( $M_{tet}^{Li} \approx 8\%$ ). Based on first-principles calculations, van der Ven and Ceder<sup>53</sup> suggested that lithium diffusion in the lithium layer of layered oxides takes place between octahedral sites via passage through the tetrahedral sites in between. However, based on the above hypotheses, at high SOC transition metals would occupy tetrahedral (reversibly) as well as octahedral (irreversibly) positions within the lithium layer, so that they would occupy the positions required for lithium diffusion, as is shown schematically in the lower panel of Scheme 1, which represents these lithium diffusion path and their blocking by transition metals. If the above discussed reversible transition metal occupancy of tetrahedral sites were to exhibit a hysteresis, i.e., if transition metal back-migration into the transition metal layer were to occur at a lower SOC along the discharge pathway compared to its migration into lithium layer tetrahedral sites during the charge pathway, the observed resistance hysteresis with respect to charge/discharge pathways could be understood.

Based on the principal mechanisms of transition metal migration on an atomic scale, we now want to turn to the effect of blocked lithium diffusion paths and its implications onto the cell resistance during

lithium re-intercalation, as shown in Figure 8. During the charge at low SOC, a rapid resistance decrease can be observed due to the rocksalt-to-spinel transition of the oxygen depleted surface layer. As one would expect, no pathway dependence is observed for this process as long as the SOC corresponds <90 mAh/g (Figure 8a). As the upper cutoff is increased to 135 mAh/g (Figure 8b), the charge resistance remains low, but now the onset of a noticeable pathway dependence can be seen during discharge, suggesting the onset of reversible TM migration. As the SOC goes beyond 60% SOC, the discharge resistance strongly increases due to reversible TM migration (Figure 8c) which has been suggested to be coupled to the anion redox phenomenon.<sup>28</sup> Assuming that TM back-migration is kinetically slow, the appearance of a strong resistance pathway dependence, namely a higher resistance during the discharge can be explained; the latter becomes even more pronounced for a higher upper SOC (Figure 8d). As the results from Figure 8 are essentially recorded within the same cycle, the hysteresis is observed at presumably the same extent of irreversible transition metal migration. This means that the resistance pathway hysteresis must be related to reversible rather than irreversible TM migration. We expect that additional irreversible migration can enhance the resistance hysteresis, but the overall phenomenon is closely coupled to reversible TM migration.

While Assat et al.<sup>43</sup> suggested based on EIS, GITT, and PITT measurements with the model compound  $\text{Li}_2\text{Ru}_{0.75}\text{Sn}_{0.25}\text{O}_3$  that the resistance pathway-dependence and the sluggish kinetics are caused by the reversible oxygen redox within the material, our data and analysis suggest that reversible cation migration might be the reason for the pathway-dependence of the resistance by blocking the lithium diffusion paths. In a recent study by Gent et al.,<sup>28</sup> the oxygen redox mechanism was closely correlated to the reversible migration of transition metals and described as dynamic process expressed as:  $\{\text{O}^{2-} + \text{TM}\} \rightarrow \{\text{O}^- + \text{TM}_{\text{mig}}\} + \text{e}^-$ . In this case, our findings and the study by Assat et al.<sup>43</sup> can be correlated, as oxygen redox and transition metal migration into tetrahedral sites of the lithium layer would both occur at high voltages (i.e., at high SOC) and thus cause the pathway-dependence and high activation energies for lithium re-intercalation. This hypothesis is supported by our observation that the pathway-dependence of the resistance only occurs at high cutoff voltages and that it can be eliminated upon complete discharge of the HE-NCM material.

Gowda et al.<sup>38</sup> carried out a detailed study on the high impedance at low SOC of Li- and Mn-rich NCMs. They observed a sharp resistance increase at low SOC which they concluded not to be caused by an interfacial resistance; in contradiction we suggest that this sharp increase is caused by a disordered surface layer that stems from oxygen release during the initial cycles. The different observation can be explained by the higher  $\text{Li}_2\text{MnO}_3$  content of 0.50 of the material used by Gowda et al.<sup>38</sup> In a previous study from Teufl et al.<sup>24</sup> it was shown that these high  $\text{Li}_2\text{MnO}_3$  contents cause oxygen release and spinel formation in the bulk material and not only at the particle surface, as shown for the material used in this study. Therefore, they could observe a higher impact of the disordered phase onto the overall impedance of the material. They also suggested that this sharp increase of the resistance at low SOC is not caused by the hysteresis, which is in one line with our observation that a disordered phase from oxygen release causes this sharp increase. While Gowda et al.<sup>38</sup> observed this sharp increase below 3.5V (equal to 40% SOC), we could only observe it below 30% SOC (see Figure 5 and Figure 8) which can be explained by the lower oxygen release expected for the material used in this study.<sup>24</sup> Furthermore, Gowda et al.<sup>38</sup> could observe a path dependent resistance >3.5 V (equal to 40% SOC) and suggested transition metal migration as possible reason which is in good accordance with the results shown in Figure 8 and the conclusions from this study.

## Conclusions

In this study we analyzed the resistance behavior of over-lithiated manganese-rich NCM (HE-NCM) at various SOC during charge and discharge and showed a correlation between structural changes,

electrochemical characteristics, and the resistance measurements. A pathway-dependent resistance hysteresis was observed during charge and discharge for HE-NCM that is activated in the first-cycle to a high upper cutoff voltage, accompanied by a large charge/discharge voltage hysteresis and a gradual voltage-fading upon extended cycling. This is not observed for a non-activated HE-NCM material, while high-voltage activation (up to 4.8V vs.  $\text{Li}^+/\text{Li}$ ) is required to achieve reasonable capacities. By a systematic variation of the upper cutoff potential for activated HE-NCM, we could show that the pathway-dependent resistance hysteresis increases with increasing upper cutoff voltages, at which the oxygen redox is believed to occur. Our data suggest that the pathway-dependence of the resistance can be rationalized by a hysteresis in the reversible transition metal migration, meaning that transition metals migrate into tetrahedral sites in the Li layer at high potentials and only migrate back into the transition metal layer upon discharge below 3V.

## Acknowledgment

The authors want to thank BASF SE who supported this work within the BASF SE Battery Research Network. Furthermore, we want to gratefully acknowledge Karin Kleiner, Benjamin Strehle, and Frederick Chesneau for very fruitful discussions and Patrick Krieg for his contribution to this work.

## ORCID

Tobias Teufl  <https://orcid.org/0000-0001-5889-5204>

Daniel Pritzl  <https://orcid.org/0000-0002-9029-107X>

Sophie Solchenbach  <https://orcid.org/0000-0001-6517-8094>

## References

- J. B. Goodenough and K. S. Park, *J. Am. Chem. Soc.*, **135**(4), 1167 (2013).
- D. Andre, S.-J. Kim, P. Lamp, S. F. Lux, F. Maglia, O. Paschos, and B. Stiaszny, *J. Mater. Chem. A*, **3**(13), 6709 (2015).
- M. M. Thackeray, C. Wolverton, and E. D. Isaacs, *Energ. Environ. Sci.*, **5**(7), 7854 (2012).
- K. Mizushima, P. Jones, P. Wiseman, and J. B. Goodenough, *Mat. Res. Bull.*, **15**(6), 783 (1980).
- J. Choi and A. Manthiram, *J. Electrochem. Soc.*, **152**(9), A1714 (2005).
- I. Belharouak, Y. K. Sun, J. Liu, and K. Amine, *J. Power Sources*, **123**(2), 247 (2003).
- Z. Lu, D. D. MacNeil, and J. R. Dahn, *Electrochem. Solid-State Lett.*, **4**(12), A200 (2001).
- M.-H. Kim, H.-S. Shin, D. Shin, and Y.-K. Sun, *J. Power Sources*, **159**(2), 1328 (2006).
- R. Jung, M. Metzger, F. Maglia, C. Stinner, and H. A. Gasteiger, *J. Electrochem. Soc.*, **164**(7), A1361 (2017).
- L. de Biasi, A. O. Kondrakov, H. Geßwein, T. Brezsesinski, P. Hartmann, and J. Janek, *J. Phys. Chem. C*, **121**(47), 26163 (2017).
- M. M. Thackeray, S.-H. Kang, C. S. Johnson, J. T. Vaughey, R. Benedek, and S. A. Hackney, *J. Mater. Chem.*, **17**(30), 3112 (2007).
- Z. Lu and J. R. Dahn, *J. Electrochem. Soc.*, **149**(7), A815 (2002).
- Z. Lu, L. Y. Beaulieu, R. A. Donabarger, C. L. Thomas, and J. R. Dahn, *J. Electrochem. Soc.*, **149**(6), A778 (2002).
- C. S. Johnson, J. S. Kim, C. Lefief, N. Li, J. T. Vaughey, and M. M. Thackeray, *Electrochem. Commun.*, **6**(10), 1085 (2004).
- F. La Mantia, F. Rosciano, N. Tran, and P. Novák, *J. Appl. Electrochem.*, **38**(7), 893 (2008).
- A. R. Armstrong, M. Holzapfel, P. Novák, C. S. Johnson, S.-H. Kang, M. M. Thackeray, and P. G. Bruce, *J. Am. Chem. Soc.*, **128**(26), 8694 (2006).
- H. Yu, H. Kim, Y. Wang, P. He, D. Asakura, Y. Nakamura, and H. Zhou, *Phys. Chem. Chem. Phys.*, **14**(18), 6584 (2012).
- J. R. Croy, M. Balasubramanian, K. G. Gallagher, and A. K. Burrell, *Acc. Chem. Res.*, **48**(11), 2813 (2015).
- D. Mohanty, J. Li, S. C. Nagpure, D. L. Wood, and C. Daniel, *MRS Energy & Sustainability*, **2**, (2015).
- N. Yabuuchi, K. Yoshii, S. T. Myung, I. Nakai, and S. Komaba, *J. Am. Chem. Soc.*, **133**(12), 4404 (2011).
- H. Koga, L. Croguennec, M. Ménétrier, P. Mannesiez, F. Weill, and C. Delmas, *J. Power Sources*, **236**, 250 (2013).
- C. Genevois, H. Koga, L. Croguennec, M. Ménétrier, C. Delmas, and F. Weill, *J. Phys. Chem. C*, **119**(1), 75 (2014).
- B. Strehle, K. Kleiner, R. Jung, F. Chesneau, M. Mendez, H. A. Gasteiger, and M. Piana, *J. Electrochem. Soc.*, **164**(2), A400 (2017).
- T. Teufl, B. Strehle, P. Müller, H. A. Gasteiger, and M. A. Mendez, *J. Electrochem. Soc.*, **165**(11), A2718 (2018).

25. E. McCalla, A. M. Abakumov, M. Saubanère, D. Foix, E. J. Berg, G. Rousse, M.-L. Doublet, D. Gonbeau, P. Novák, G. Van Tendeloo, D. R., and J. M. Tarascon, *Science*, **350** (6267), 1516 (2015).
26. H. Koga, L. Croguennec, M. Menetrier, K. Douhil, S. Belin, L. Bourgeois, E. Suard, F. Weill, and C. Delmas, *J. Electrochem. Soc.*, **160**(6), A786 (2013).
27. D. H. Seo, J. Lee, A. Urban, R. Malik, S. Kang, and G. Ceder, *Nat. Chem.*, **8**(7), 692 (2016).
28. W. E. Gent, K. Lim, Y. Liang, Q. Li, T. Barnes, S.-J. Ahn, K. H. Stone, M. McIntire, J. Hong, J. H. Song, Y. Li, A. Mehta, S. Ermon, T. Tyliczszak, D. Kilcoyne, D. Vine, J.-H. Park, S.-K. Doo, M. F. Toney, W. Yang, D. Prendergast, and W. C. Chueh, *Nat. Commun.*, **8**(1), 2091 (2017).
29. M. Jiang, B. Key, Y. S. Meng, and C. P. Grey, *Chem. Mater.*, **21**(13), 2733 (2009).
30. H. Liu, Y. Chen, S. Hy, K. An, S. Venkatachalam, D. Qian, M. Zhang, and Y. S. Meng, *Adv. Energy Mater.*, **6**(7), 1502143 (2016).
31. D. Mohanty, A. S. Sefat, J. Li, R. A. Meisner, A. J. Rondinone, E. A. Payzant, D. P. Abraham, D. L. Wood 3rd, and C. Daniel, *Phys. Chem. Chem. Phys.*, **15**(44), 19496 (2013).
32. D. Mohanty, J. Li, D. P. Abraham, A. Huq, E. A. Payzant, D. L. Wood, and C. Daniel, *Chem. Mater.*, **26**(21), 6272 (2014).
33. M. Sathiya, A. M. Abakumov, D. Foix, G. Rousse, K. Ramesha, M. Saubanere, M. L. Doublet, H. Vezin, C. P. Laisa, A. S. Prakash, D. Gonbeau, G. VanTendeloo, and J. M. Tarascon, *Nat. Mater.*, **14**(2), 230 (2015).
34. A. van Bommel, L. J. Krause, and J. R. Dahn, *J. Electrochem. Soc.*, **158**(6), A731 (2011).
35. K. Kleiner, B. Strehle, A. R. Baker, S. J. Day, C. C. Tang, I. Buchberger, F.-F. Chesneau, H. A. Gasteiger, and M. Piana, *Chem. Mater.*, **30**(11), 3656 (2018).
36. M. Bettge, Y. Li, K. Gallagher, Y. Zhu, Q. Wu, W. Lu, I. Bloom, and D. P. Abraham, *J. Electrochem. Soc.*, **160**(11), A2046 (2013).
37. K. G. Gallagher, S.-H. Kang, S. U. Park, and S. Y. Han, *J. Power Sources*, **196**(22), 9702 (2011).
38. S. R. Gowda, D. W. Dees, A. N. Jansen, and K. G. Gallagher, *J. Electrochem. Soc.*, **162**(7), A1374 (2015).
39. W. Mao, G. Ai, Y. Dai, Y. Fu, X. Song, H. Lopez, and V. Battaglia, *J. Electrochem. Soc.*, **163**(14), A3091 (2016).
40. J. Zheng, W. Shi, M. Gu, J. Xiao, P. Zuo, C. Wang, and J. G. Zhang, *J. Electrochem. Soc.*, **160**(11), A2212 (2013).
41. S.-H. Kang, W.-S. Yoon, K.-W. Nam, X.-Q. Yang, and D. P. Abraham, *J. Mater. Sc.*, **43**(14), 4701 (2008).
42. H. Yu, Y. Wang, D. Asakura, E. Hosono, T. Zhang, and H. Zhou, *RSC Adv.*, **2**(23), 8797 (2012).
43. G. Assat, C. Delacourt, D. A. D. Corte, and J.-M. Tarascon, *J. Electrochem. Soc.*, **163**(14), A2965 (2016).
44. S. Solchenbach, D. Pritzl, E. J. Y. Kong, J. Landesfeind, and H. A. Gasteiger, *J. Electrochem. Soc.*, **163**(10), A2265 (2016).
45. H. G. Schweiger, O. Obeidi, O. Komesker, A. Raschke, M. Schiemann, C. Zehner, M. Gehnen, M. Keller, and P. Birke, *Sensors (Basel)*, **10**(6), 5604 (2010).
46. D. Pritzl, A. Bumberger, M. Wetjen, J. Landesfeind, S. Solchenbach, and H. Gasteiger, *J. Electrochem. Soc.*, **166**(4), A582 (2019).
47. J. Landesfeind, D. Pritzl, and H. A. Gasteiger, *J. Electrochem. Soc.*, **164**(7), A1773 (2017).
48. M. Gaberscek, J. Moskon, B. Erjavec, R. Dominko, and J. Jamnik, *Electrochem. Solid-State Lett.*, **11**(10), A170 (2008).
49. J. Landesfeind, J. Hattendorff, A. Ehrl, W. A. Wall, and H. A. Gasteiger, *J. Electrochem. Soc.*, **163**(7), A1373 (2016).
50. J. R. Croy, K. G. Gallagher, M. Balasubramanian, Z. Chen, Y. Ren, D. Kim, S.-H. Kang, D. W. Dees, and M. M. Thackeray, *J. Phys. Chem. C*, **117**(13), 6525 (2013).
51. P. G. Bruce, A. R. Armstrong, and L. Gitzendanner, *J. Mater. Chem.*, **9**, 193 (1998).
52. M. M. Thackeray, *Prog. Solid State Chem.*, **25**, 1 (1997).
53. A. Ven and G. Ceder, *J. Power Sources*, **97**, 529 (2001).
54. I. Buchberger, S. Seidlmayer, A. Pokharel, M. Piana, J. Hattendorff, P. Kudejova, R. Gilles, and H. A. Gasteiger, *J. Electrochem. Soc.*, **162**(14), A2737 (2015).
55. S.-H. Kang, D. P. Abraham, W.-S. Yoon, K.-W. Nam, and X.-Q. Yang, *Electrochim. Acta*, **54**(2), 684 (2008).
56. J. R. Croy, K. G. Gallagher, M. Balasubramanian, B. R. Long, and M. M. Thackeray, *J. Electrochem. Soc.*, **161**(3), A318 (2014).
57. F. Dogan, B. R. Long, J. R. Croy, K. G. Gallagher, H. Iddir, J. T. Russell, M. Balasubramanian, and B. Key, *J. Am. Chem. Soc.*, **137**(6), 2328 (2015).